Superior compressive performance of hierarchical origami-corrugation metallic sandwich structures based on selective laser melting

Bin Han [a,*,1], Zengshen Yue [b,c,d,1], Hao Wu [a], Qi Zhang [a], Tian Jian Lu [c,d,*]

[a] School of Mechanical Engineering, Xi'an Jiaotong University, Xi'an 710049, PR China
[b] State Key Laboratory for Strength and Vibration of Mechanical Structures, Xi'an Jiaotong University, Xi'an 710049, PR China
[c] State Key Laboratory of Mechanics and Control of Mechanical Structures, Nanjing University of Aeronautics and Astronautics, Nanjing 210016, PR China
[d] Nanjing Center for Multifunctional Lightweight Materials and Structures (MLMS), Nanjing University of Aeronautics and Astronautics, Nanjing 210016, PR China

ARTICLE INFO

ABSTRACT

Novel hierarchical origami-corrugation metallic sandwich (HOCM) structures have been proposed, by replacing the facets of the Miura-Ori patterned foldcore with smaller-scale corrugated sandwiches. A series of as-fabricated and after-heated samples were additively manufactured from two high-strength metals (i.e., IN718 and 17-4PH) by selective laser melting (SLM) technique. The microstructure of HOCM samples, and the post-fracture of parent materials were characterized. Quasi-static out-of-plane compressive behavior of the HOCM structures was experimentally and numerically investigated, with an excellent agreement between the measurements and FE simulations. Effects of relative density and parent material (especially the heat treatment) on the compressive properties were explored in terms of deformation mechanism, compressive strength and energy absorption. The layer-by-layer small-scale folding deformation dominating in the crushing process contributes to a relatively high and long stress-plateau stage, which leads to the excellent energy absorption. The heat treatment of the HOCM samples increases the compressive strength, but might not benefit the energy absorption. The IN718 and 17-4PH hierarchical origami-corrugation metallic sandwiches exhibit very competitive mechanical properties compared to cellular topologies, and possess great potential as lightweight load-bearing and energy-absorbent engineering components.

1. Introduction

Mechanical metamaterials have received increasing attention since their superior or counterintuitive mechanical properties and even multifunctional integration [1–5], which originate in the rationally designed geometric architectures instead of the properties of each component [6–8]. Mechanical metamaterials usually share curious fancy but feasible mechanical properties, e.g., ultralight, ultra-stiffness/strength, well-controllable flexibility, negative compressibility and negative Poisson's ratio [9–13], with multifunctional portability ranging from vibration suppression to optimal ferroelectric properties [14–19]. Ultralight mechanical metamaterials with ultra-stiffness/strength and great energy absorption are of great potential to replace traditional monolithic plates or beams in a wide range of engineering applications, e.g., load-bearing, blast and impact resistance [9,20–23]. Among the ultralight metamaterials, origami-inspired mechanical

metamaterials (creating 3D structures from 2D sheets through a process of folding along creases) could offer enhanced flexibility, deformability and compactness, emulating the principles of paper folding and translating them to the design of new materials and advanced application ranging from space exploration to automotive safety, biomedical devices and extremely foldable and stretchable electronics [24–27]. The classic Miura-Ori tessellated pattern consisting of identical parallelogram facets surrounding the vertices of a degree of 4 [27,28], as the most widely studied type of origami structures, has recently been proposed as a kind of origami mechanical metamaterial exhibiting low weight, negative (in-plane) Poisson's ratios, design flexibility and some other features (e. g., bi-stability and multi-stability) [1,13,25], though it was proposed about 45 years ago [29].

Moreover, Miura-Ori and its derivatives have fairly high specific stiffness and specific strength which is comparable with traditional 2D lattice structures, like corrugations and honeycombs. Because of the
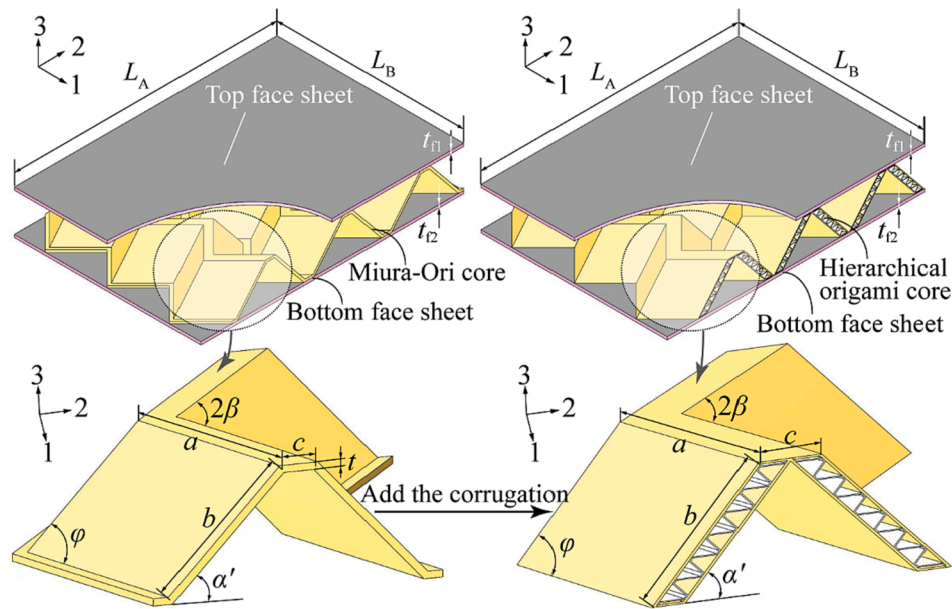

Fig. 1. Geometric configurations of the Miura-Ori sandwich (left) and the novel hierarchical origami-corrugation metallic sandwich (right), with the corresponding unit cell of the foldcores shown at the bottom.

existence of open channels, Miura-Ori does not suffer from the moisture accumulation problem, which often is inevitable for honeycombs [30]. Miura-Ori mechanical metamaterials can potentially be applied as the sandwich cores in engineering applications attributed to the high stiffness-to-weight ratio, open ventilation channels, continuous manufacturing process, great energy absorption and impact resistance [31–35]. Zhou et al. [30] conducted a parametric study on the mechanical properties of a variety of Miura-based folded sandwich core models virtually tested in quasi-static out-of-plane compression, shear, and bending using the finite element (FE) method, and found that the Miura-Ori cores had comparable or even better shear and bending performances, but was a little weaker in out-of-plane compression compared with honeycombs. Subsequently, the aluminum foldcores as sandwich structures were built and tested in out-of-plane compression, shear, bending and impact by Fischer [31], and showed comparable mechanical properties as aluminum foam and honeycomb. Lv et al. [32] focused on the out-of-plane compressive performance of the Miura-Ori patterned sheets and their corresponding sandwich panels, to examine their load-carrying capacity and the energy absorption capacity. Zhang et al. [36] then studied the in-plane quasi-static large deformation compressive behavior of the Miura-Ori based metamaterials and found they could outperform honeycombs with the same relative density in in-plane energy absorption capability; Karagiozova et al. [37] studied the dynamic in-plane compression of Miura-Ori metamaterials and noted their potential application in dynamic resistance. Inspired by this, Harris and McShane [38,22] proposed metallic stacked origami cellular materials with attractive properties by stacking layers of Miura-folded origami sheets, which exhibited good performances in terms of both strength and energy absorption. Briefly speaking, it can be concluded from the related literature that the Miura-Ori-based metamaterials exhibit potential mechanical properties though with a little bit weak energy absorption capability along the out-of-plane direction, since the out-of-plane compressed Miura-Ori metamaterials usually collapse by buckling and folding with a rapid softening after the peak strength, and densify at a lower nominal strain.

Recently, there is growing booming interest in the research of either hierarchical or hybrid design of ultralight cellular structures and metamaterials to strengthen and expand their mechanical properties. A well-known example of engineered architecture, the Eiffel Tower, demonstrates the possibility of superior architectural enhancement with

a relatively low density and a robust mechanical performance attributed to the hierarchical lattice design [39]. Kooistra et al. [40] proposed the concept of the hierarchical corrugated sandwich panel and found that such sandwich made from structural alloy showed significantly higher compressive and shear strengths than the first-order counterparts with equal mass, for the case of relative densities less than about 5%. In addition, a hierarchical honeycomb metamaterial was constructed, by replacing the cell walls of the regular honeycombs with hexagonal, Kagome, and triangular lattices [41], to obtain the improved in-plane dynamic energy absorption capability. Dong [42] manufactured Ti-6Al-4V hierarchical architected lattice metamaterials by a snap-fit assembling technique with a subsequent vacuum brazing operation, achieving superior compressive modulus and strength. Zhang et al. [43] developed hierarchical sheet triply periodic minimal surface (TPMS) lattices with the lattice walls consisting of successively smaller scale TPMS architectures, which could achieve a wide range of controllable geometric properties and have higher resistance against buckling at ultralow densities than the first-order counterparts. Based on the hybrid reinforcement concept [44], Yan et al. [45] made efforts to enhance the compressive behavior of the corrugated sandwich panels by filling the aluminum foam into the lattice gaps, which obtained the enhancement $(1 + 1 \gg 2)$ on the compressive strength and energy absorption. Similar results were demonstrated by Han et al. [46], who selected honeycomb-corrugation hybrid as a novel sandwich core, which exhibited superiority in both strength and energy absorption in the low-density regime. Overall, the hierarchy and hybrid design strategy are of great significance to the enhancement of ultralight cellular materials. However, the development of either hierarchical or hybrid metamaterials with complicated and multiscale architectures is still challenging as hindered by limitations in manufacturing techniques. While additive manufacturing (AM) enables the direct and efficient fabrication of complex geometries including all kinds of metamaterials, biomimetic structures and hierarchical cellular or lattice structures, from a range of metal alloys, polymers and ceramics [47,48], and thus would greatly promote the development of hierarchical metamaterials with superior mechanical properties and multifunctionalities.

Integrating the concept of structural hierarchy and hybrid, we propose a novel hierarchical origami-corrugation metallic sandwich (HOCM) structure by replacing the facets of the Miura-Ori patterned sandwich core with smaller-scale corrugated sandwich panels (see
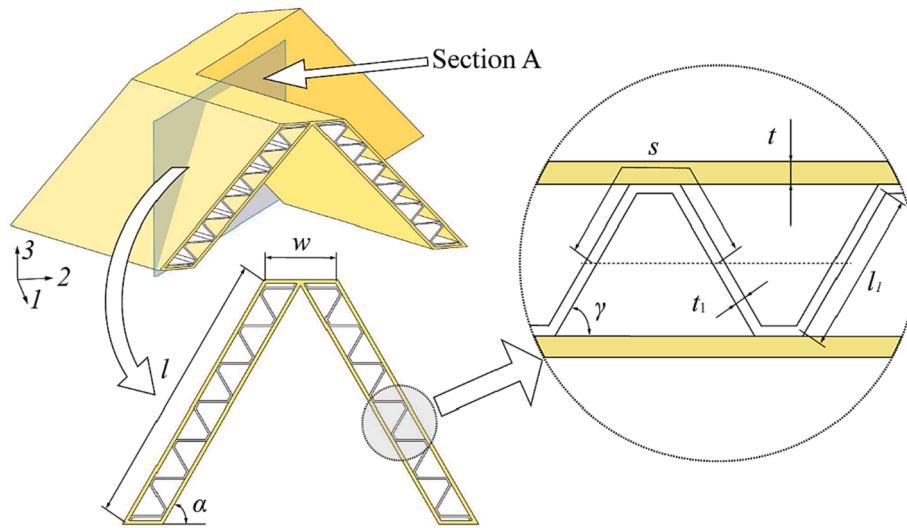
Fig. 2. Schematic of the second-order topology of HOCM, with geometric parameters defined in the cross-section perpendicular to the parallelogram facet.

Fig. 1), expecting to obtain superior compressive mechanical properties. A series of as-fabricated and after-heated samples were additively manufactured from two high-strength metals (i.e., Ni-based superalloy IN718 and stainless steel 17-4PH) by selective laser melting (SLM) technique, and tested under the out-of-plane compression, and the corresponding full model finite element (FE) simulations were conducted to analyze the compressive performance in detail. This paper is organized as follows: Section 2 characterizes the geometry design, manufacturing, and samples of the HOCM structures. Section 3 describes the experimental and simulated methodology. The mechanical properties and post-fracture analysis of the as-built and after-heated parent metals are discussed in Section 4. In Section 5, the compressive performance of HOCMs is discussed from the experimental and numerical results, and the performance comparison with competing topologies is included.

2. Design and manufacturing

2.1. Topology design

As shown in Fig. 1, the hierarchical origami-corrugation metallic sandwich (HOCM) is developed from the origami sandwich with Miura-Ori patterned foldcores, of which have small platforms ensuring a good connection of foldcores with face sheets [35]. Such hierarchical architected sandwich core structure has a hierarchical order of 2 and contains two levels of length scale, with Miura-Ori topology for the large-scale architecture (first-order), and corrugated sandwich panels for the small-scale (second-order) architecture to replace the parallelogram facets of Miura-Ori foldcores. The unit cell of the first-order Miura-Ori topology is determined by 6 parameters independently, consisting of length and width of the parallelogram facets a, b, width of the platform c, angle between the inclination edge of parallelogram facets and the horizontal line α', folding angle β, thickness of facets t. The relationship of the parallelogram sector angle φ with α', and β is given as:

$$\cos\varphi = \cos\alpha' \cdot \cos\beta, \tag{1}$$

$$\sin^2\varphi = \sin^2\alpha' + \cos^2\alpha' \cdot \sin^2\beta. \tag{2}$$

As for the HOCM, the second-order architecture (i.e., the corrugated sandwich) is characterized by inclination angle γ, corrugation thickness t_1, corrugation length l_1, half wavelength s, and facet thickness t, as illustrated in Fig. 2. The parameter relationships of the first-order topology and the second architecture of HOCM follow:

$$\tan\alpha' = \tan\alpha \cdot \sin\beta, \tag{3}$$

$$w = c \cdot \sin\beta = \frac{2(l_1 \cdot \sin\gamma + 2t + t_1)}{\sin\alpha}, \tag{4}$$

$$l = b \cdot \sin\varphi, \tag{5}$$

where α and l denote separately the inclination angle and the height of facets, and w is the nominal width of the platform, which are all defined in the cross-section perpendicular to parallelogram facets.

Therefore, the HOCM structure could be determined independently by 9 parameters, including a, l, t, l_1, t_1, s, α, β and γ, which imply a very large degree of design freedom. The relative density $\bar{\rho}$ of the HOCM could be expressed as:

$$\bar{\rho} = \frac{2\left\{ 2lt + lt_1 \left[\frac{s}{s + (\cos\gamma - 1)l_1} \right] + \frac{2(l_1 \cdot \sin\gamma + 2t + t_1)t}{\sin\alpha} \right\}}{l[a \cdot \sin\alpha \cdot \sin\beta \cdot \cos\beta + 2l \cdot \sin\alpha \cdot \cos\alpha + 2(l_1 \cdot \sin\gamma + 2t + t_1)]}. \tag{6}$$

2.2. Fabrication

2.2.1. Selective laser melting

The HOCM structures of parent materials were additively manufactured by selective laser melting (SLM) technique using a 3DS-300 SLM machine (3D System, America). Two metallic powders, i.e., Ni-based superalloy IN718 and stainless steel 17-4PH were selected with the chemical composition listed in Table 1, which were supplied by AVI-METAL Powder Metallurgy Technology China. The average particle size of IN718 is approximately 30 μm, while that of 17-4PH is approximately 40 μm, both with good spheroidization. As for the printing parameters of

Table 1
The chemical composition of IN718 and 17-4PH powders (unit: wt.%).

IN718	Ni	Cr	Nb	Mo	Ti	Al	C	Si & Mn & Cu	Fe
	50 ~ 55	17 ~ 21	4.75 ~ 5.5	2.8 ~ 3.3	0.65 ~ 1.15	0.2 ~ 0.8	≤0.08	≤0.35	Bal.
17-4PH	C	Si	Mn	P	S	Ni	Cr	Cu	Nb & Ta	Fe
	≤0.07	≤1	≤1	≤0.04	≤0.03	3 ~ 5	15 ~ 17.5	3 ~ 5	0.15 ~ 0.45	Bal.

Table 2
Heat treatment of the SLM samples made of IN718 and 17-4PH (AC: air cooling, FC: Furnace cooling).

Parent material	Heat treatment process		
	Solution treatment	Aging	Secondary aging
IN718	1040℃/2h/AC	720℃/8h/FC	620℃/8h/AC
17-4PH	1040℃/1h/AC	720℃/4h/AC	None

SLM, the IN718 skin layer was printed with a laser power of 75 W and a scanning speed of 800 mm/s, and the inner region with a laser power of 305 W and a scanning speed of 960 mm/s for ease removal of samples from the workbench; while 17-4PH samples were printed with the laser power of 150 W and the scanning speed of 1200 mm/s throughout the whole processing. After SLM processing, half of the as-fabricated samples were heat-treated, with the parameters as shown in Table 2.

2.2.2. Specimens and microstructure

Table 3 lists the geometrical parameters of all the HOCM samples, which were tested in the present study. Due to the limitation of printing size, HOCM samples only consist of two unit-cells of the first-order Miura-Ori topology, as shown in Fig. 3. The ratio of thickness of facet to corrugation is set to be 1 for all the samples. It should be noted that for the naming of samples (details refer to the notes of Table 3), **t1**, **t2**, and **t3** were selected to distinguish the thickness of samples, however, did not represent the exact values of thickness. For example, the thickness of **if-nh-t2** is 0.74 mm, while the thickness of sample **sf-nh-t2** is 0.95 mm. Typical HOCM specimens are illustrated in Fig. 3a, of which the hierarchical origami-corrugation cores are clearly presented in Fig. 3b. To evaluate the fabrication quality, the scanning electron microscopy (SEM, SU3500, Hitachi, Japan) technique was carried out. Figure 3d shows the microstructure of Region A marked in Fig. 3c. It is found that the sample surface is relatively flat without any micro-voids or micro-cracks, which implies good manufacturing quality. In addition, the sample was cut along Line B as shown in Fig. 3c, by wire-cut electro-discharge machining (EDM), which enabled the SEM observation of the inner parallelogram facet as presented in Fig. 3e. It can be seen that the inter-surface of the parallelogram facet is relatively denser with only a small amount of un-melted metal powders marked by black dashed lines, and has better surface roughness, in contrast to Region A. This means that the HOCM samples fabricated by SLM in the present study have fewer defects.

3. Experimental and simulation methodology

3.1. Material testing

Dog-bone tensile coupons of IN718 and 17-4PH were printed using identical SLM processing parameters of HOCM samples. Half of the dog-bone specimens were heat-treated as described in Table 2. Uniaxial tensile tests were carried out on both the as-fabricated and after-heated dog-bone specimens at the ambient temperature with a nominal strain rate of 1×10^{-3} s^{-1} using an MTS machine (MTS-858 Mini Bionix, MTS Corporation, USA). The applied force was obtained from the load cell and deformation was recorded by an extensometer simultaneously. For accuracy, each testing set was repeated six times, and the average data was adopted. To further explore qualitatively the influence of the post-printing heat treatment, the fracture surfaces of the dog-bone samples after tensile testing were observed by SEM analysis; afterwards, the energy-dispersive X-ray spectroscopy (EDS) analysis was carried out to evaluate the components of the second-phase particles in the fracture surface for both 17-4PH and IN718 after heating treatment.

3.2. Quasi-static compressive tests of hierarchical origami-corrugation metallic sandwiches

Quasi-static out-of-plane compression tests of HOCM samples were carried out at a nominal strain rate of 5.96×10^{-4} s^{-1} by the same MTS machine, as sketched in Fig. 4. Compressive loading was exerted along the 3-direction by the upper platen, with the lower platen fixed. Two digital image correlation (DIC) cameras were set in front of the sandwich sample along the 2-direction for the surface displacement field collection, from which the evolution of the strain field could be calculated (only applied for Sample **if-ph-t1**, which would be discussed in Section 5.3.2 in detail); while a digital video was set at the other side of the samples along the 1-direction to record the deformation process of samples. For the measurement of the DIC system, the speckle pattern was applied to the surface of samples facing the two cameras: firstly, the surface was sprayed with white paint as background, and then a pattern of 1–3 mm diameter black dots was employed to cover approximately 50% area of the surface randomly [49]. The nominal compressive strain was calculated as the ratio of the loading displacement and the height of HOCM samples; while the nominal compressive stress was obtained as the ratio of loading force and the area of the sandwich face sheet. In the experiments, for each set of parameters, two samples were prepared and tested for HOCM structure. It has been established that the compressive responses for the sandwich specimens in each set are quite repeatable.

3.3. Finite element modeling

To further reveal the mechanical properties and failure process of the HOCM structures under out-of-plane compression, full model finite element (FE) simulations were carried out using ABAQUS v6.16/Explicit. Geometric parameters of FE models are the same as the tested HOCM specimens. The HOCM models were discretized using linear quadrilateral shell elements with reduced integration (S4R), with an average element size of $l_1/8$, which was found to satisfy both numerical accuracy and computing efficiency. The HOCM model was compressed
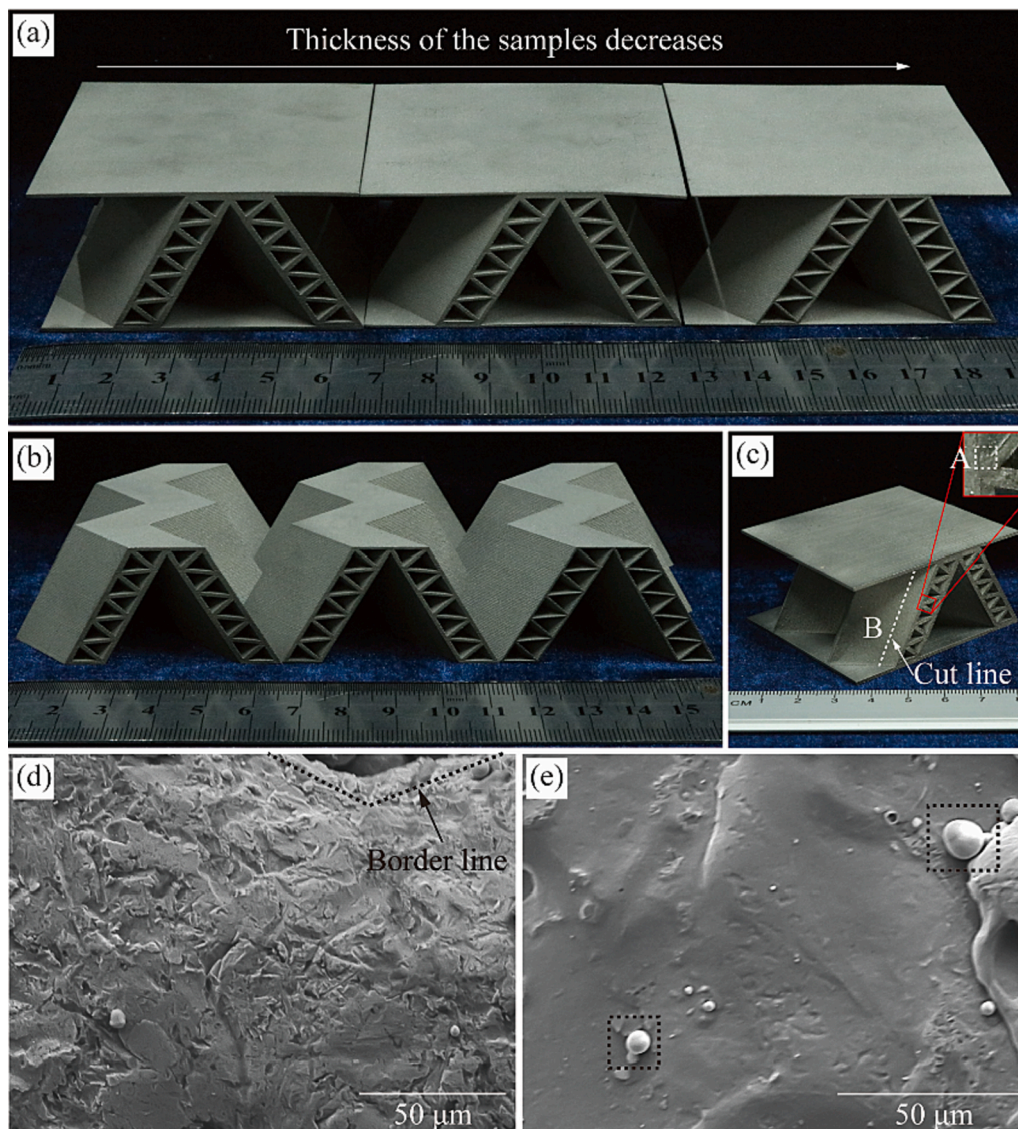
Table 3
Geometric parameters of all HOCM samples (note that: for the naming of samples, **if** represents samples fabricated by IN718, while **sf** refers to those fabricated by 17-4PH steel; **nh** denotes no heating treatment, while **ph** implies post-heating treatment; **t1**, **t2**, and **t3** are employed to distinguish the thickness of samples).

Sample No.	a (mm)	l (mm)	l_1 (mm)	t (mm)	t_1 (mm)	s (mm)	α	β	γ	$\overline{\rho}$
if-nh-t1 **if-ph-t1** **sf-nh-t1** **sf-ph-t1**	20	27.24	6	0.60	0.60	6	67.79°	45°	60°	0.124
if-nh-t2 **if-ph-t2**	20	27.24	6	0.74	0.74	6	67.79°	45°	60°	0.152
if-nh-t3 **if-ph-t3** **sf-nh-t2** **sf-ph-t2**	20	27.24	6	0.95	0.95	6	67.79°	45°	60°	0.194

Fig. 3. Images of the as-fabricated IN718 HOCM samples: (a) hierarchical origami-corrugation metallic sandwich structures; (b) hierarchical origami-corrugation sandwich core; (c) sample schematic for SEM; SEM image of (d) Region A and (e) the surface of the inner parallelogram facet as-cut along with Line B as shown in (c).

between two rigid pressure platens, of which the bottom plate was fixed, and the top one was moved along the 3-direction (see Fig. 4) at a sufficiently slow speed to ensure that the simulated crushing response is quasi-static. General contact was employed for all the simulations with a fixed Coulomb friction coefficient of 0.3.

In this paper, only the as-built IN718 HOCM samples (without heat treatment) were considered for FE simulations. IN718 without heat treatment as the parent material was modeled as isotropic elastic–plastic solid and obeyed the von Mises J2-flow theory without consideration of material damage. The material parameters employed in the simulation were obtained from the tensile tests of dog-bone specimens: the elastic behavior of the parent material was modeled using the parameters listed in Table 4 with the Poisson's ratio $\nu = 0.3$ [50], while the plasticity was simulated using the true strain–stress data calculated from the measured data shown in Fig. 5.

4. Constituent material characterization

4.1. Mechanical properties

Figure 5 presents the tensile mechanical performance of the parent materials, i.e., the as-built and after-heated IN718 and 17-4PH, with the detail of specimen naming given in the figure note. For each case, six dog-bone specimens were tested to obtain the average engineering stress-true strain curve. Generally speaking, the heat treatment for both IN718 and 17-4PH significantly improves the mechanical properties of the parent material. Corresponding material properties, i.e., Young's modulus E_s, yield strength $\sigma_{0.2}$ (0.2% elastic offset), ultimate strength σ_u, and elongation are summarized in Table 4. It is seen that after the heat treatment, yield strength and ultimate strength are obviously enhanced (especially for IN718), Young's modulus increases a little, but the elongation is decreased. Moreover, the ultimate strengths of both IN718 and 17-4PH after the heat treatment using the process parameters listed in Table 2 are apparently superior to those reported in other literature [51,52], while the elongations are comparable.
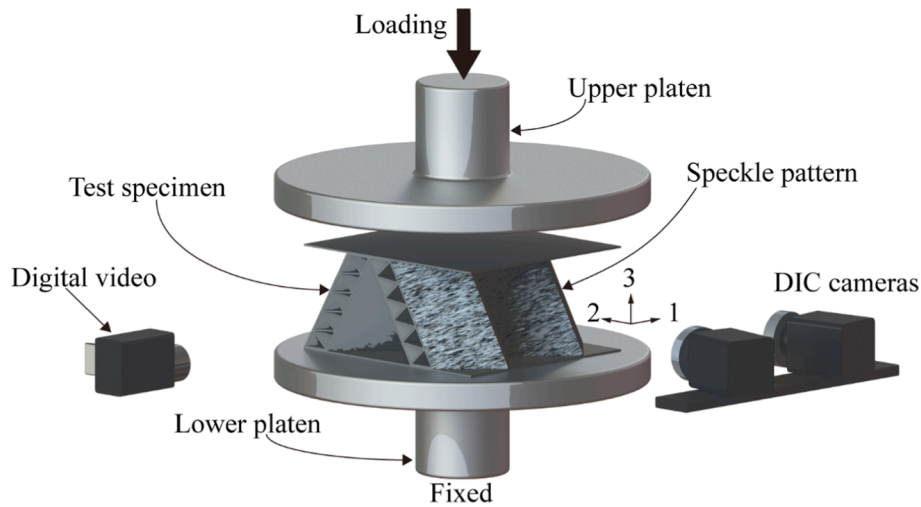
Fig. 4. Schematic of the hierarchical metallic sandwich specimen under out-of-plane compression with the DIC system for the surface displacement field measurement, and the digital video for recording the deformation process.

Table 4
Measured mechanical properties of parent materials in the current study and comparison with those from literature. The notes of **i-nh**, **s-nh**, **s-ph** and **i-ph** refer to that of Fig. 5.

Material	Density ρ_s (g/cm³)	Young's modulus E_s (GPa)	Yield strength $\sigma_{0.2}$ (MPa)	Ultimate strength σ_u (MPa)	Elongation (%)
i-nh	8.24	144.51	815.16	1296.11	18.02
i-ph	8.24	160.70	1469.98	1783.27	13.01
IN718 heat-treated [51]	8.24	/	1140 ± 30	1280 ± 20	17 ± 1
s-nh	7.80	187.77	807.08	1436.89	27.98
s-ph	7.80	192.39	857.00	1517.79	14.09
17-4PH heat-treated [52]	7.80	/	870 ± 25	1358 ± 8	13.3 ± 1.5

Fig. 5. Measured tensile engineering stress versus engineering strain curve of the SLM fabricated metal materials. Note that **i** is for IN718, and **s** for 17-4PH stainless steel; **nh** denotes no heat treatment, **ph** refers to post-heating treatment.

4.2. Post-fracture analysis

For qualitatively revealing the influencing mechanism of the heat treatment, the fracture morphology of the dog-bone samples after tensile testing was observed by SEM, as shown in Fig. 6a,b,d,e. Despite the differences in material strength and elongation, tiny dimples could be observed on all the fracture surfaces of the as-built and post-heated IN718 and 17-4PH, corresponding to ductile rupture. However, the dimples of the as-built metals materials without heat treatment seem to be deeper and denser than those of the after-heated ones, which implies better ductility of the as-built samples. In addition, the brittle cleavages are apparently observed on the fracture surface of the after-heated IN718 sample, corresponding to the lowest elongation among the four types of samples. Furthermore, the extra difference between the as-built and post-heated fracture surfaces concentrates on the second-phase particles. The IN718 and 17-4PH samples after heat treatment both have more and larger second-phase particles, in which the beneficiation of Cu was both observed from the EDS analysis (see Fig. 6c,f). Consequently, both the yield and ultimate strength increase but the elongation decreases after the heat treatment.
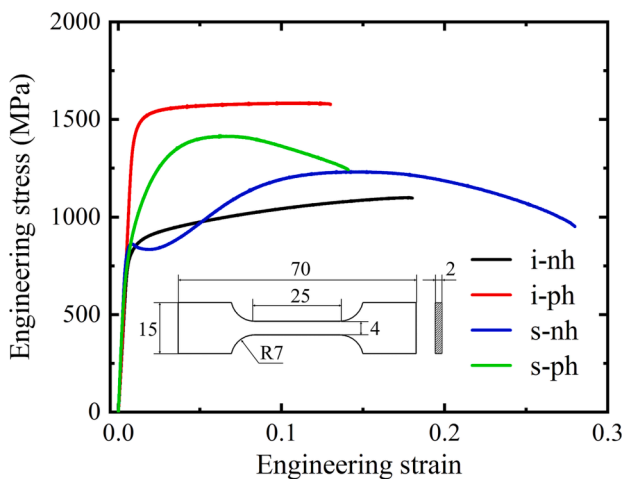
5. Compressive performance of hierarchical origami-corrugation metallic sandwiches

5.1. Mechanical behavior of hierarchical origami-corrugation metallic sandwiches

To characterize the compressive behavior of hierarchical origami-corrugation metallic sandwich, Fig. 7 presents the typical out-of-plane compressive stress–strain curve for Sample **if-nh-t1** (the as-built IN718 HOCM sample with the smallest facet thickness, see Table 3) from both experiment and simulation, with the corresponding deformation process illustrated in Fig. 8. It is shown from Fig. 7 that the simulated compressive stress–strain curve of the sample compares quite well with the measured curve. As presented in Fig. 8, the simulated deformation evolution of the compressed HOCM is almost identical to that observed in the experiment. The coincidence of simulations with experiments can be also similarly found for other HOCM samples (as shown in Fig. 10, Fig. 11, Fig. 12 for the later discussion). Quantitatively, the peak strength and energy absorption (calculated up to a compressive strain of 0.5: $E_V = \int_0^{0.5} \sigma_n \varepsilon_n d\varepsilon_n$; σ_n: nominal stress, ε_n: nominal strain) are summarized in Table 5. It can be seen that all the percentage differences between FE simulations and experimental measurements for both peak strength and energy absorption are less than
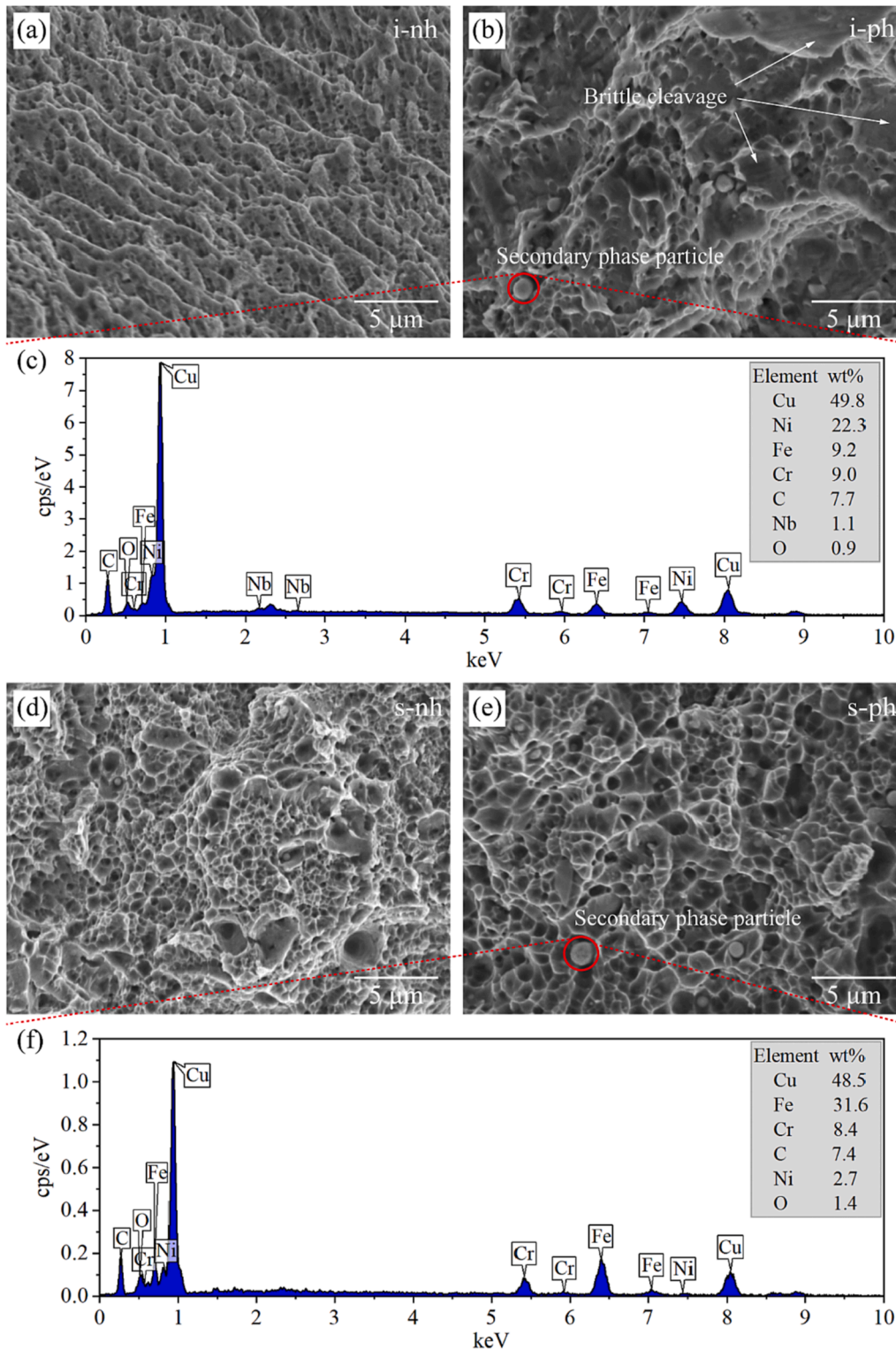
Fig. 6. SEM micrographs taken from the tensile fracture surfaces of (a) **i-nh** sample, (b) **i-ph** sample, (d) **s-nh** sample, and (e) **s-ph** sample. The EDS analysis of the second-phase particle as marked in (b) and (e) is separately presented in (c) and (f).

10%. This implies that the present FE models could accurately mimic the compressive performance of the HOCM samples. However, slight difference exists between the simulations and the tests. The small deviation in the first peak strength mainly results from the defects induced during fabrication, e.g., uneven distribution of surface roughness (see Fig. 3d, e) and facet thickness, and some micro defects. The slight mismatch of the fluctuations in the plateau region of the stress–strain curves is probably

attributed to influences of the contact stiffness of testing machine in the initial loading, and the inevitable slight randomness of contact regions in the compressive process.

In this section, the mechanical performance of HOCM is explored by the combination of experiment and simulation. It can be seen from Fig. 7 that the compressive curve exhibits an initial linear response region firstly, and then a nonlinear response till a peak strength; after that, a
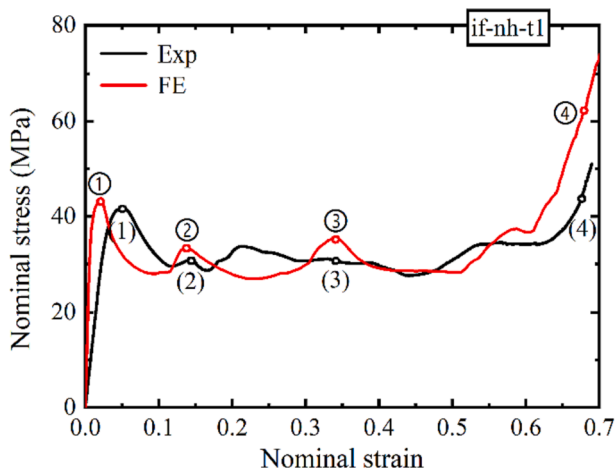
Fig. 7. Compressive stress–strain curves of Sample **if-nh-t1** from both experiment and simulation.

sudden softening is observed, followed by an approximate plateau region with slight fluctuations till the densification. Overall, the compressive behavior of HOCM can be divided into three stages: the initial collapse, the crushing process, and densification, of which the first two stages would be separately discussed in detail to explore the collapse mechanism.

5.1.1. Initial collapse

The numerically simulated initial collapse response of HOCM is presented in Fig. 9a with representative deformation configurations given in Fig. 9b. Following an initial elastic compression at small strain,

bifurcation deviating from the linear elastic response occurs at Point ① in Fig. 9a, which corresponds to the local plastic yielding in the upper intersection region of the outer convex facets and the bottom intersection region of the inner concave facets (Configuration ① in Fig. 9b). This is attributed to the first stress concentration of the fold-line region near the connection between the first-order Miura-Ori core and face sheet. Subsequently, as the curve entered a nonlinear region from point ① to point ②, plastic yielding rapidly expands along the diagonal lines (marked by red dotted lines), and the diagonal yielding region is increased to other corners as shown in Configuration ②. With further compression up to point ③, the peak stress is reached; almost all the facets yield, while most of the corrugations remain elastic (Configuration ③). Afterwards, a gradual softening follows due to localized plastic buckling of the facets (Configuration ④ of Fig. 9b), which would evolve to the localized collapse under further compression. Notably, the local deformation is antisymmetric from the side view (marked by red dotted ellipses Configuration ④).

5.1.2. Crushing process

Following the initial collapse, the crushing behavior with plastic folding deformation dominates with the compressive strain exceeding 0.1, as shown in Figs. 7 and 8. Both the experimental and simulated folding configurations are presented in Fig. 8. After the local plastic buckling as shown in Configuration (1) and ①, the first localized fold with plastic hinges starts to form. With the increase of compressive strain, the contact of the local facets and the corrugations emerges at the folding region with the expansion of plastic hinges (configuration (2) and ②), which corresponds to the first slightly fluctuation in the curve (Point (2) and ② in Fig. 7). Afterwards, the plastic folding deformation continues to expand and the small-scale folds pile up layer by layer (see Configuration (3) and ③), which contributes to an approximate long-plateau stage with slight fluctuations in the compressive curve
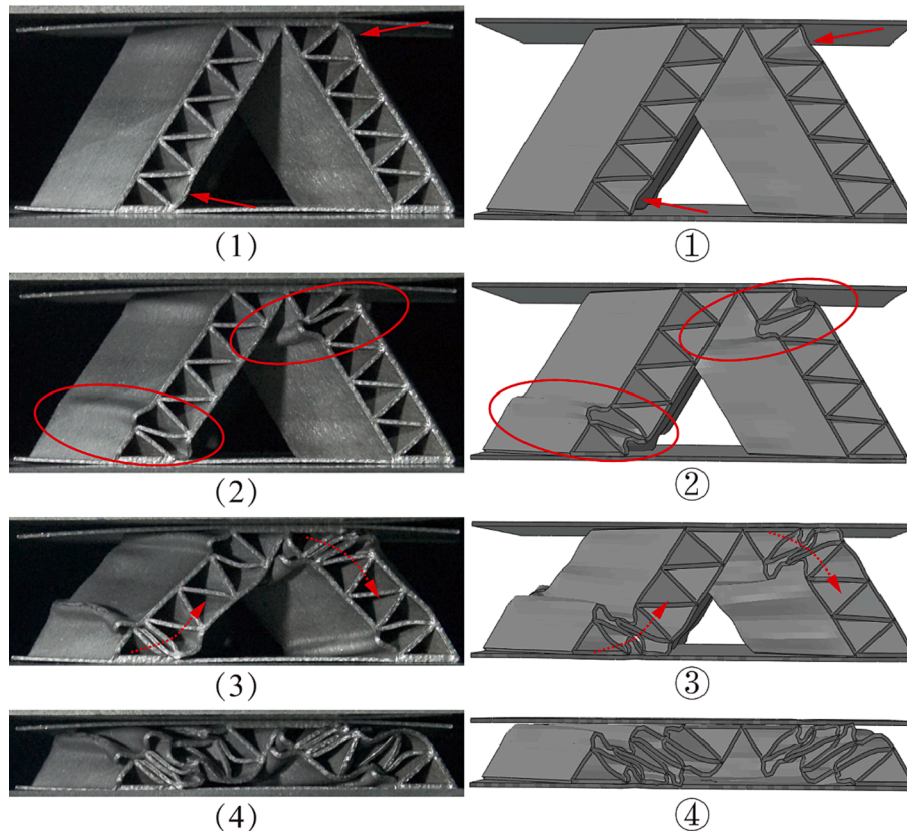

Fig. 8. Representative deformation configurations of Sample **if-nh-t1** from both experiment and simulation at different stages of crushing, corresponding to numbered bullets marked on the curves of Fig. 7.
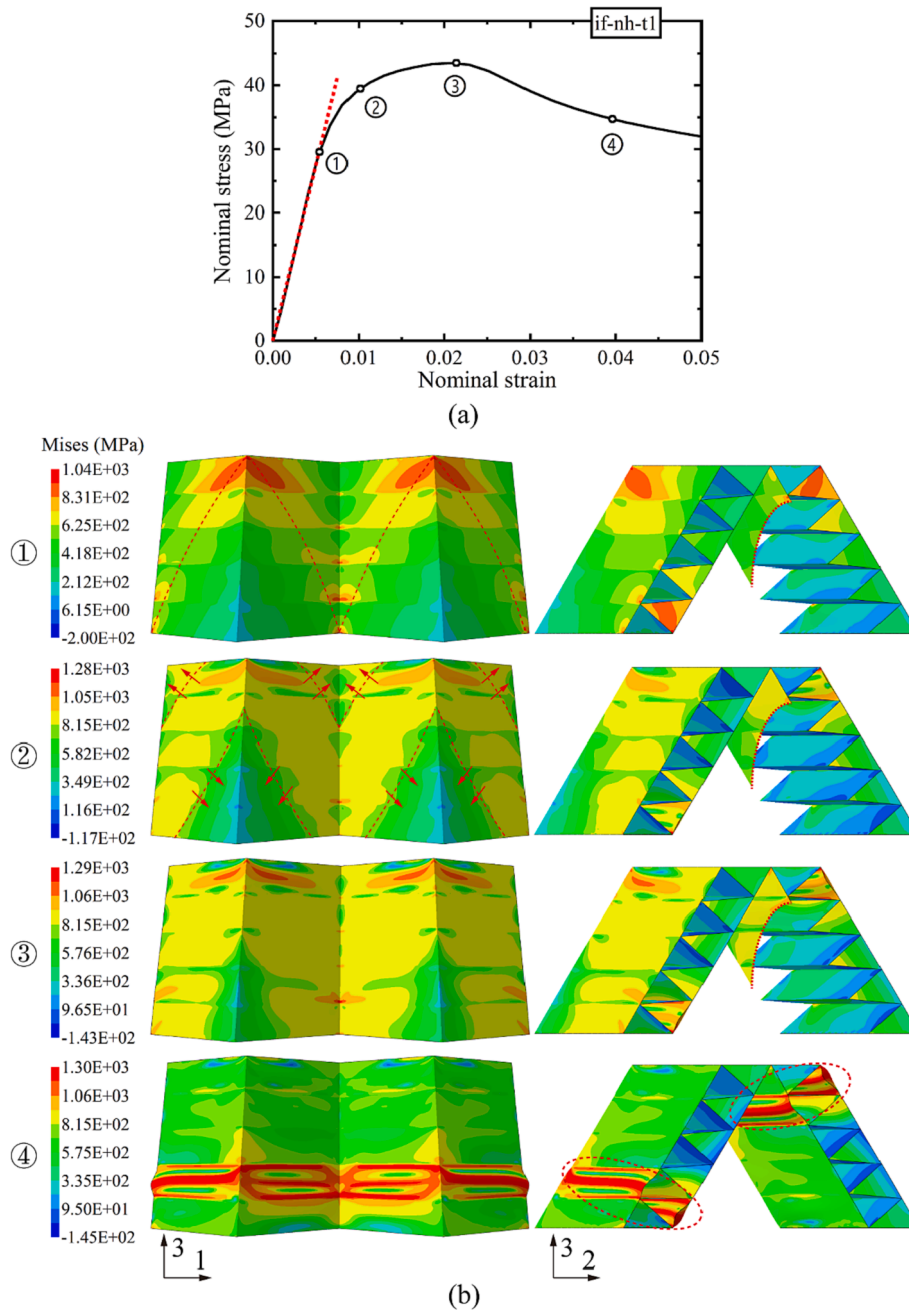
Fig. 9. Initial collapse behavior of Sample **if-nh-t1**: (a) simulated initial stress–strain response; (b) corresponding deformation configurations, corresponding to numbered bullets marked on the curve of (a). For better observation, the inner facets in the first three configurations are partially cut.

(Fig. 7). As the HOCM was compressed to densification, seriously stacked folds and contacting deformations could be obviously observed in Configuration (4) and ④.

For the Miura-Ori foldcore under out-of-plane compression [31,32], it usually collapses by single buckling and folding on the first-order Miura-Ori topology with a rapid softening after the peak strength, and densifies at a lower compressive strain, which corresponds to a little bit weak energy absorption capacity along the out-of-plane direction. Differently, the hierarchical origami-corrugation metallic sandwich core collapses by the layer-by-layer small-scale folding deformation, with a relatively high and long stress-plateau stage and the onset strain of densification up to 65%, which would contribute to the excellent energy absorption under out-of-plane compression.

5.2. Effect of the relative density

By increasing the facet thickness (the same as the corrugation thickness), two other as-built IN718 HOCM samples, i.e., **if-nh-t2**, **if-nh-t3**, were also tested under out-of-plane compression. Including **if-nh-t1**, the three samples without heat treatment all have different relative densities, which are controlled by the facet thickness as listed in Table 3. Figure 10 presents the measured and simulated compressive stress––strain curves of **if-nh-t2** and **if-nh-t3**. The FE calculations compare well with the experiments for both samples. Compared to the curve of **if-nh-t1** in Fig. 7, the softening after the first peak stress is less obvious for **if-nh-t2**, and almost disappears for **if-nh-t3**. Moreover, as the relative density increases, the fluctuations in the stress-plateau stage gradually diminish, while the onset strain of densification seems to decrease a little.
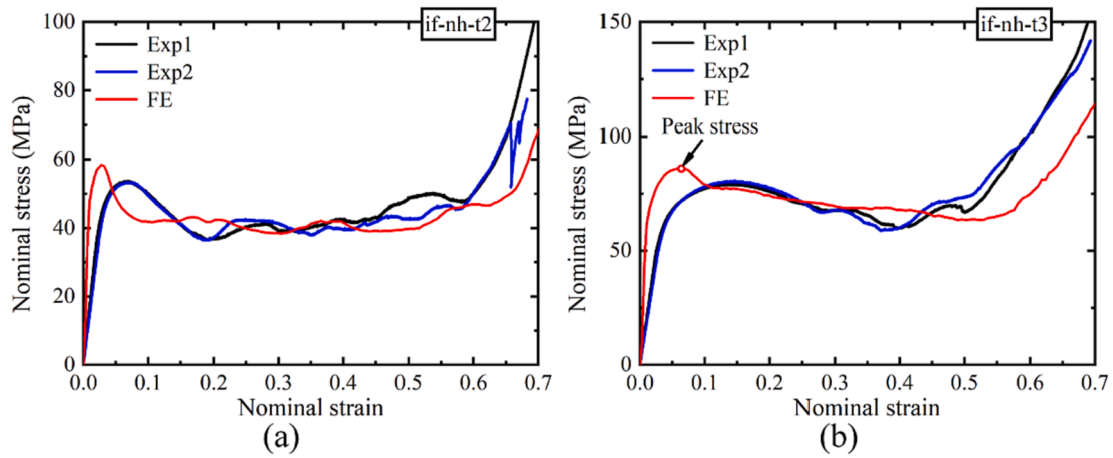
Fig. 10. Compressive stress–strain curves from both experiments and simulations for as-built HOCM samples: (a) **if-nh-t2**, (b) **if-nh-t3**.
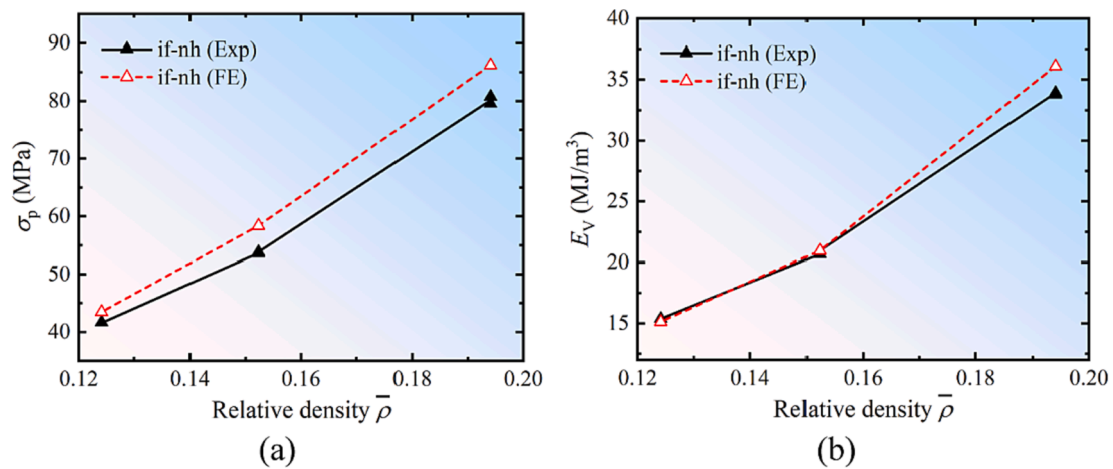

Fig. 11. The effect of relative density on (a) compressive strength and (b) energy absorption for as-built IN718 HOCM samples (without heat treatment).
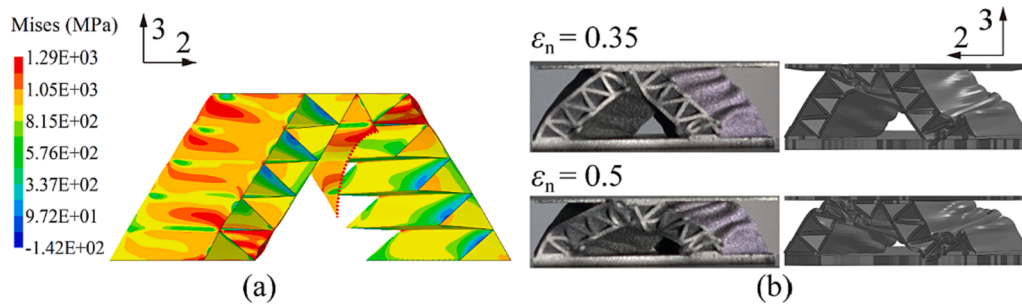

Fig. 12. Deformation details of Sample **if-nh-t3**: (a) Contour of the von-Mises stress at first peak stress as marked in Fig. 10b; (b) deformation configurations at the compressive strain of 35% and 50%.

Table 5
Compressive peak strength and energy absorption of HOCM samples: comparison between experimental measurements and FE calculated results.

Sample No.	Peak strength (MPa)					Energy absorption (MJ/m^3)				
	Experiments			FE simulations	Error (%)	Experiments			FE simulations	Error (%)
	Exp1	Exp2	Average			Exp1	Exp2	Average		
if-nh-t1	41.68	--	41.68	43.49	4.34	15.40	--	15.40	15.15	−1.62
if-nh-t2	53.75	53.51	53.63	58.37	8.84	20.95	20.66	20.81	20.96	0.72
if-nh-t3	79.47	80.69	80.08	86.22	7.67	33.78	33.92	33.85	36.09	6.62

Note: the errors are calculated from the average values of experimental measurements and the FE simulated results.
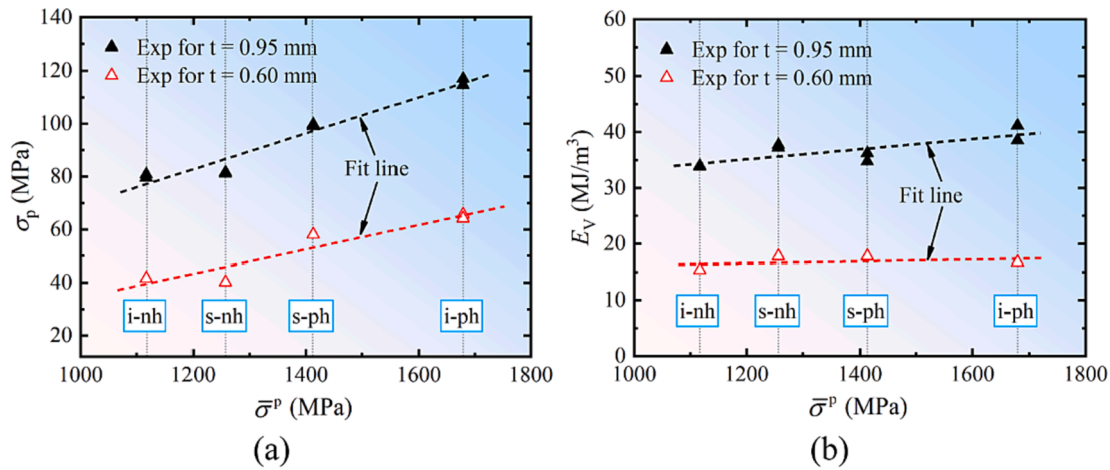
Fig. 13. Experimentally measured (a) compressive strength and (b) energy absorption of the HOCM structures, as functions of the mean value of plastic flow stress $\bar{\sigma}^p$. The notes of **i-nh**, **s-nh**, **s-ph** and **i-ph** refer to that of Fig. 5.

The effect of the relative density on the compressive strength and energy absorption of HOCMs is illustrated in Fig. 11. As is shown, with the increase of relative density, both the compressive strength and energy absorption obviously increase by nearly 100% and 133%, respectively. This is possibly attributed to the gradual disappearance of the post-peak softening for HOCM with large relative density, which results in much higher plateau stress benefiting the energy absorption.

To further explore the change in compressive behavior, deformation details of Sample **if-nh-t3** with the thickest facets are presented in Fig. 12. It is found from Fig. 12a that, besides the facets, most regions of the corrugations yield at the peak stress, which is different from Sample **if-nh-t1**. This implies that the corrugations seem to provide much stronger support for the parallelogram facets under the initial compression. In addition, it is revealed from Fig. 12b that the stacked folding deformation dominates in the crushing process for Sample **if-nh-t3**, which is more or less similar to that of Sample **if-nh-t1** (see Fig. 8). Differently, the corrugated panel of second-order topology in Sample **if-nh-t1** is barely deformed, while that in Sample **if-nh-t3** exhibits higher
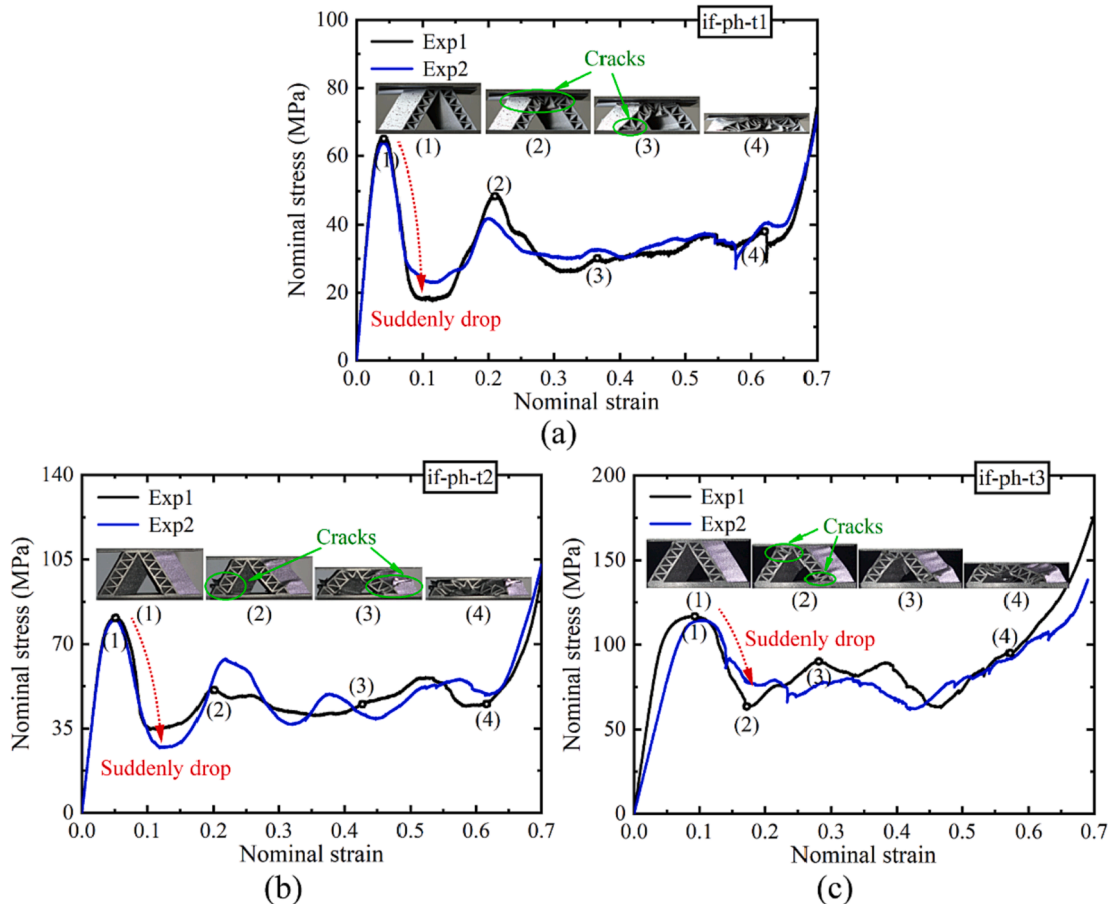

Fig. 14. Compressive stress–strain curves of post-heated HOCM samples: (a) **if-ph-t1**, (b) **if-ph-t2**, and (c) **if-ph-t3**, with corresponding deformation configurations as marked on the curves. Notes of sample naming refer to that of Table 3.
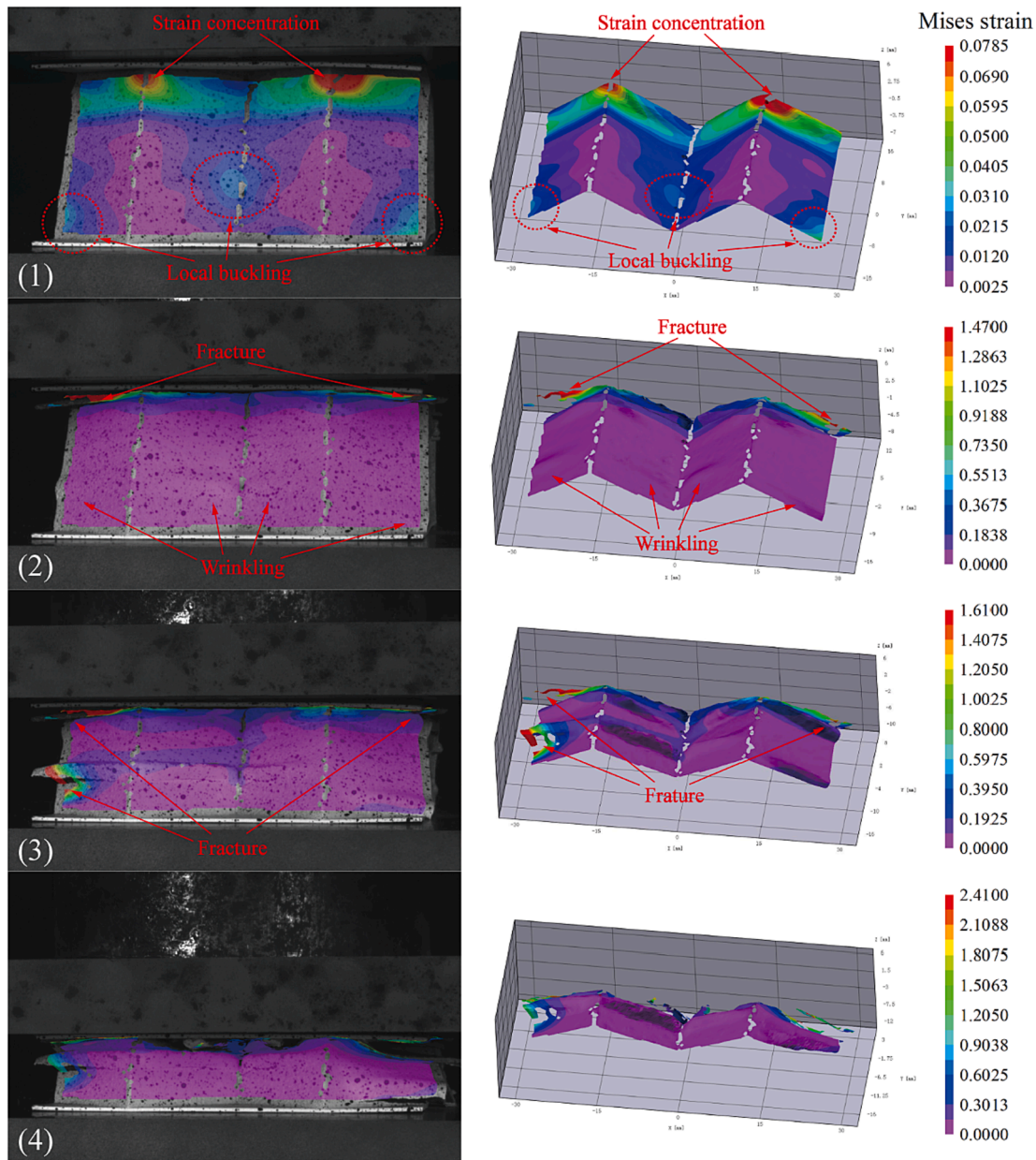
Fig. 15. Surface Mises-strain fields of the parallelogram facets calculated from the DIC measurement for Sample **if-ph-t1** at selected compressive strains as marked in Fig. 14.

participation in the plastic folding deformation at large compressive strain, which might also contribute to the better smoothness in the plateau stage of the compressive stress–strain curve.

5.3. Effect of the parent materials

5.3.1. Constituent material

The as-built and post-heated HOCM samples made of IN718 and 17-4PH were all fabricated and tested under out-of-plane compression. According to the above analysis of as-built IN718 samples, it is known that the compressive behavior of HOCM is mainly dominated by the plastic deformations of structural components. As is known, both the constituent and the heat treatment of parent materials influence the plastic flow of the tensile curves (see Fig. 5). Thus, to explore the effect of the parent material on the compressive performance of tested HOCM structures, the mean value of plastic flow stress [53] is introduced by

$$\overline{\sigma}^{\mathrm{p}} = \frac{\int_0^{\varepsilon_0^{\mathrm{p}}} \sigma(\varepsilon^{\mathrm{p}}) \mathrm{d}\varepsilon^{\mathrm{p}}}{\varepsilon_0^{\mathrm{p}}}, \tag{7}$$

where ε^{p} denotes the true plastic strain and σ is the true stress, both calculated from the tensile curves of parent materials in Fig. 5. Moreover, $\varepsilon_0^{\mathrm{p}}$ is defined as a characteristic plastic strain, which is chosen as the value of fracture strain minus elastic strain.

As shown in Fig. 13, the effect of the parent material on both compressive strength and energy absorption could be quantitatively presented as functions of $\overline{\sigma}^{\mathrm{p}}$. The results demonstrate that both compressive strength and energy absorption increase almost linearly with the increase of $\overline{\sigma}^{\mathrm{p}}$, which means that stronger parent material endows better compressive properties of HOCM. Interestingly, the increasing trend of both compressive strength and energy absorption, reflected by the slope of the fit line, is sensitive to the facet thickness of HOCMs: the slope for HOCMs with thicker facets is much larger than
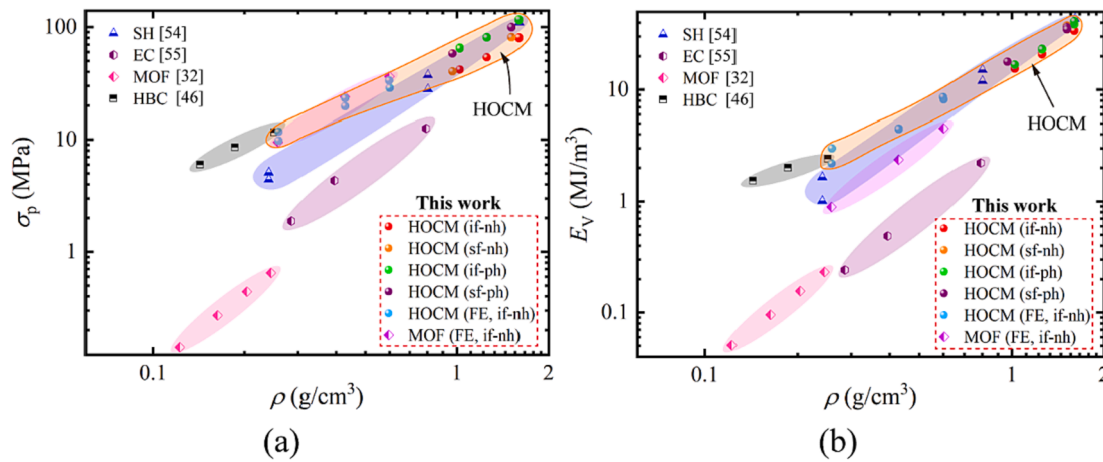
Fig. 16. Performance of HOCM structures with competing sandwich topologies: (a) compressive strength versus core density; (b) energy absorption versus core density. **i-nh**, **s-nh**, **s-ph** and **i-ph** refer to the parent materials as defined in the note of Fig. 5.

that for HOCMs with thinner facets, which implies the compressive properties of the latter HOCMs is less sensitive to the parent material. Especially, HOCMs made of different parent materials, with the facet thickness of 0.6 mm almost share the same energy absorption. This might be partly attributed to the low participation of small-scale corrugated panels with small thickness in the initial collapse and the plastic folding deformation of the crushing process, as discussed in Section 5.2. Moreover, worse ductility of the parent material after the heat treatment weakens the energy absorption of thinner-walled HOCMs, which is discussed in detail next.

5.3.2. Compressive behaviors after the heat treatment

To further explore the effect of heat treatment on compressive behaviors of HOCMs, Fig. 14 presents the compressive stress–strain curves of the heat-treated IN718 samples (i.e., **if-ph-t1**, **if-ph-t2**, and **if-ph-t3**), with typical deformation configurations included. In contrast to the results of as-built samples displayed in Figs. 7 and 10, although the first peak stress is obviously increased, much more serious softening with a sudden drop occurs after the peak stress, which corresponds to the local buckling and initiation of cracks. As the compression continues, the localized cracks propagate rapidly, accompanied by the formation of new cracks (see the deformation configurations as shown in Fig. 14). This contributes to the large fluctuations of the stress-plateau stage. Although the yield and ultimate strengths of IN718 are both greatly increased after the heat treatment, the stress-plateau stage of the after-heated HOCMs increases little or even decreases slightly compared to the as-built IN718 samples with the same geometric parameters, due to the worse ductility of post-heated parent material. In other words, the heat treatment could increase the compressive strength, but might not benefit the energy absorption.

The above discussion can be further demonstrated by the evolution of 3D effective strain fields on the facet surfaces of Sample **if-ph-t1** calculated from the DIC measurement, as shown in Fig. 15. At the peak stress (see Image (1)), plastic strain concentrates on the top edge near the crease line, and localized buckling (circled by the red dash lines) occurs on the parallelogram facets, which would evolve to the wrinkling and folding deformation at larger compressive strain (see Images (2) and (3)). The obvious fracture at the top edge can be found in Image (2) with the effective strain up to the elongation of the heat-treated IN718 (13%, Table 4). Subsequently, cracks propagate and new cracks form, with larger plastic folding deformation layer by layer (as shown in Image (3),

which would continue until the densification (see Image (4)). For the HOCM samples after heat treatment, the crushing process is dominated by the combination of layered plastic folding deformation and material fracture.

5.4. Performance comparison with competing topologies

The mechanical properties of the hierarchical origami-corrugation metallic sandwiches are compared with other competing sandwich core topologies, as shown in Fig. 16. In the material selection maps, the compressive strength and energy absorption are plotted as functions of the density of different cellular materials. These include 304 stainless steel square honeycombs (SH) [54], 304 stainless steel empty corrugations (EC) [55], aluminum Miura-Ori patterned foldcores (MOF) [32], aluminum honeycomb-corrugation hybrid composite structures (HBC) [46] and the present IN718 and 17-4PH hierarchical origami-corrugation metallic sandwich (HOCM) structures from experiments. Moreover, the numerically calculated HOCMs and Miura-Ori foldcores with equal mass, both made of IN718 without heat treatment, are also included, of which the detailed geometrical parameters are presented in the **Appendix**. Energy absorption is commonly taken up to the compressive strain of 0.5. However, because the IN718 Miura-Ori fold-cores (MOF) from present simulations tend to densify at a lower nominal strain (with the onset densification strain less than 50%), performance metrics are computed up to densification only for these materials.

It is noted from Fig. 16 that, the performance of HOCMs in terms of either compressive strength and energy absorption is quite appealing. The IN718 and 17-4PH HOCMs outperform 304 stainless steel empty corrugations, aluminum Miura-Ori patterned foldcores, and are comparable to aluminum honeycomb-corrugation hybrid composite structures and 304 stainless steel square honeycombs. Specifically, comparison between IN718 HOCM and IN718 MOF with equal density demonstrates that the compressive strength of HOCM is comparable to that of MOF, while HOCM obviously outperforms MOF in terms of energy absorption. This is because that replacing the parallelogram faces with smaller-scale corrugated sandwiches could lead to a relatively higher and longer stress-plateau stage, which contributes to the superiority of energy absorption. Moreover, the hierarchical feature of HOCM across different length scales would endow larger design flexibility of controllable geometric properties including multiscale porosities and significantly increased surface areas, which could be applied

for multifunctional applications such as heat transfer and active cooling. Meanwhile, they avoid the problem of water accumulation in closed-cell structures such as honeycombs.

6. Conclusions

A novel hierarchical origami-corrugation metallic sandwich (HOCM) structure with superior compressive performance has been presented in this paper. A sequence of as-fabricated and after-heated samples was additively manufactured from two high strength metals (i.e., IN718 and 17-4PH) by selective laser melting (SLM) technique. The microstructure of HOCM samples, and the post-fracture of parent materials were discussed. Quasi-static out-of-plane compressive behavior of the HOCM structures was investigated using a combined approach of experimental measurements and numerical simulations. Main conclusions are summarized as follows:

- The IN718 and 17-4PH HOCM structures can be made by selective laser melting, with good surface quality. As for both IN718 and 17-4PH as the parent materials, the yield and ultimate strength increase but the elongation decreases after the heat treatment, due to the increase of the quantity and size of the second-phase particles.
- Under out-of-plane compression, the as-built HOCM (without heat treatment) initially collapses by localized plastic buckling, and subsequently deforms by the layer-by-layer small-scale folding deformation in the crushing process, with a relatively high and long stress-plateau stage, which contributes to the excellent energy absorption. While for the after-heated HOCM samples, the crushing process is dominated by the combination of layered plastic folding deformation and the material fracture.
- With the increase of relative density, both the compressive strength and energy absorption of HOCM obviously increase by nearly 100% and 133%, respectively. The parent material also plays an important role in the compressive strength and energy absorption of the HOCM structures. Worse ductility of the parent material after the heat treatment weakens the energy absorption of thinner-walled HOCMs.
- Compared to other cellular materials, the hierarchical origami-corrugation metallic sandwich structures made of IN718 and 17-4PH exhibit very competing mechanical properties, which are comparable to aluminum honeycomb-corrugation hybrid composite structures and 304 stainless steel square honeycombs. As for such hierarchical topology, the compressive strength is comparable to that of Miura-Ori foldcore (MOF) with equal density, but the energy absorption is more superior.

The current research sheds lights on the potential of 3D printed hierarchical origami-corrugation metallic sandwich structures as lightweight load-bearing and energy-absorbent engineering components. The structural superiority would not only exhibit in compression, but also in shear, bending and other loadings, which would be explored in further study. Such hierarchical architecture across different length scales also endows a larger design flexibility of controllable geometric properties including multiscale porosities and significantly increased surface areas, which could be applied for multifunctional applications such as heat transfer and active cooling.

CRediT authorship contribution statement

Bin Han: Conceptualization, Methodology, Funding acquisition, Writing – review & editing. **Zengshen Yue:** Methodology, Investigation, Software, Visualization, Writing – original draft. **Hao Wu:** Investigation. **Qi Zhang:** Resources, Funding acquisition. **Tian Jian Lu:** Supervision, Funding acquisition, Writing – review & editing.

Declaration of Competing Interest

The authors declare that they have no known competing financial interests or personal relationships that could have appeared to influence the work reported in this paper.

Data availability

The raw/processed data required to reproduce these findings cannot be shared at this time as the data also forms part of an ongoing study.

Acknowledgments

Appendix A

For the additional FE simulations in Fig. 16, geometric parameters of IN718 HOCMs and MOFs without heat treatment are listed in Table A1. The relative density is small, with the range of 0.03–0.07. Since for MOF with larger density, the facet thickness t exceeds 4 mm, which would result in the serious material fracture of SLM-printed MOF under compression, even for the as-built IN718 without heat treatment. This would lead to bad fidelity of the prediction from the FE simulations, which ignored the material damage.

Table A1

Geometric parameters of the additionally calculated HOCMs and MOFs, both made of as-built IN718 without heat treatment (i.e., **i-nh**).

Sample No.	a (mm)	l (mm)	l_1 (mm)	t (mm)	t_1 (mm)	s (mm)	α	β	γ	$\bar{\rho}$
HOCM-1–1	100	76	4	0.500	0.500	5	60°	45°	60°	0.03
HOCM-1–2	100	76	4	0.320	0.640	5	60°	45°	60°	0.03
HOCM-2–1	100	76	4	0.828	0.828	5	60°	45°	60°	0.05
HOCM-2–2	100	76	4	0.530	1.060	5	60°	45°	60°	0.05
HOCM-3–1	100	76	4	1.160	1.160	5	60°	45°	60°	0.07
HOCM-3–2	100	76	4	0.740	1.480	5	60°	45°	60°	0.07
MOF-1	100	76	–	1.775	–	–	60°	45°	–	0.03
MOF-2	100	76	–	2.940	–	–	60°	45°	–	0.05
MOF-3	100	76	–	4.120	–	–	60°	45°	–	0.07

References

[1] Zadpoor AA. Mechanical meta-materials. Mater Horiz 2016;3:371–81. https://doi.org/10.1039/C6MH00065G.

[2] Bertoldi K, Vitelli V, Christensen J, van Hecke M. Flexible mechanical metamaterials. Nat Rev Mater 2017;2:1–11. https://doi.org/10.1038/natrevmats.2017.66.

[3] Frenzel T, Kadic M, Wegener M. Three-dimensional mechanical metamaterials with a twist. Science 2017;358:1072–4. https://doi.org/10.1126/science.aao4640.

[4] Chen Y, Jia Z, Wang L. Hierarchical honeycomb lattice metamaterials with improved thermal resistance and mechanical properties. Compos Struct 2016;152:395–402. https://doi.org/10.1016/j.compstruct.2016.05.048.

[5] Li X, Yu X, Chua JW, Lee HP, Ding J, Zhai W. Microlattice metamaterials with simultaneous superior acoustic and mechanical energy absorption. Small 2021;17:2100336. https://doi.org/10.1002/smll.202100336.

[6] Sha Y, Jiani L, Haoyu C, Ritchie RO, Jun X. Design and strengthening mechanisms in hierarchical architected materials processed using additive manufacturing. Int J Mech Sci 2018;149:150–63. https://doi.org/10.1016/j.ijmecsci.2018.09.038.

[7] Overvelde JTB, Bertoldi K. Relating pore shape to the non-linear response of periodic elastomeric structures. J Mech Phys Solids 2014;64:351–66. https://doi.org/10.1016/j.jmps.2013.11.014.

[8] Greer JR, Park J. Additive manufacturing of nano- and microarchitected materials. Nano Lett 2018;18:2187–8. https://doi.org/10.1021/acs.nanolett.8b00724.

[9] Zheng X, Lee H, Weisgraber TH, Shusteff M, DeOtte J, Duoss EB, et al. Ultralight, ultrastiff mechanical metamaterials. Science 2014;344:1373–7. https://doi.org/10.1126/science.1252291.

[10] Li T, Chen Y, Hu X, Li Y, Wang L. Exploiting negative Poisson's ratio to design 3D-printed composites with enhanced mechanical properties. Mater Des 2018;142:247–58. https://doi.org/10.1016/j.matdes.2018.01.034.

[11] Bodaghi M, Damanpack AR, Hu GF, Liao WH. Large deformations of soft metamaterials fabricated by 3D printing. Mater Des 2017;131:81–91. https://doi.org/10.1016/j.matdes.2017.06.002.

[12] Meza LR, Das S, Greer JR. Strong, lightweight, and recoverable three-dimensional ceramic nanolattices. Science 2014;345:1322–6. https://doi.org/10.1126/science.1255908.

[13] Yu X, Zhou J, Liang H, Jiang Z, Wu L. Mechanical metamaterials associated with stiffness, rigidity and compressibility: a brief review. Prog Mater Sci 2018;94:114–73. https://doi.org/10.1016/j.pmatsci.2017.12.003.

[14] Li J, Fan X, Li F. Numerical and experimental study of a sandwich-like metamaterial plate for vibration suppression. Compos Struct 2020;238:111969. https://doi.org/10.1016/j.compstruct.2020.111969.

[15] Wu W, Hu W, Qian G, Liao H, Xu X, Berto F. Mechanical design and multifunctional applications of chiral mechanical metamaterials: a review. Mater Des 2019;180:107950. https://doi.org/10.1016/j.matdes.2019.107950.

[16] Shi J, Akbarzadeh AH. Hierarchical cellular ferroelectric metamaterials: a design motif to enhance multifunctional figures of merit. Compos Struct 2020;250:112395. https://doi.org/10.1016/j.compstruct.2020.112395.

[17] Jia Z, Liu F, Jiang X, Wang L. Engineering lattice metamaterials for extreme property, programmability, and multifunctionality. J Appl Phys 2020;127(15):150901. https://doi.org/10.1063/5.0004724.

[18] Wei K, Xiao X, Chen J, Wu Y, Li M, Wang Z. Additively manufactured bi-material metamaterial to program a wide range of thermal expansion. Mater Des 2021;198:109343. https://doi.org/10.1016/j.matdes.2020.109343.

[19] Shi J, Akbarzadeh AH. 3D Hierarchical lattice ferroelectric metamaterials. Int J Eng Sci 2020;149:103247. https://doi.org/10.1016/j.ijengsci.2020.103247.

[20] Yazdani Sarvestani H, Akbarzadeh AH, Mirbolghasemi A, Hermenean K. 3D printed meta-sandwich structures: failure mechanism, energy absorption and multi-hit capability. Mater Des 2018;160:179–93. https://doi.org/10.1016/j.matdes.2018.08.061.

[21] Chen Y, Li T, Jia Z, Scarpa F, Yao C-W, Wang L. 3D printed hierarchical honeycombs with shape integrity under large compressive deformations. Mater Des 2018;137:226–34. https://doi.org/10.1016/j.matdes.2017.10.028.

[22] Harris JA, McShane GJ. Impact response of metallic stacked origami cellular materials. Int J Impact Eng 2021;147:103730. https://doi.org/10.1016/j.ijimpeng.2020.103730.

[23] Mohsenizadeh M, Gasbarri F, Munther M, Beheshti A, Davami K. Additively-manufactured lightweight Metamaterials for energy absorption. Mater Des 2018;139:521–30. https://doi.org/10.1016/j.matdes.2017.11.037.

[24] Zhai Z, Wang Y, Jiang H. Origami-inspired, on-demand deployable and collapsible mechanical metamaterials with tunable stiffness. Proc Natl Acad Sci 2018;115:2032–7. https://doi.org/10.1073/pnas.1720171115.

[25] Silverberg JL, Na J-H, Evans AA, Liu B, Hull TC, Santangelo CD, et al. Origami structures with a critical transition to bistability arising from hidden degrees of freedom. Nat Mater 2015;14:389–93. https://doi.org/10.1038/nmat4232.

[26] Fang H, Chu S-C-A, Xia Y, Wang K-W. Programmable self-locking origami mechanical metamaterials. Adv Mater 2018;30:1706311. https://doi.org/10.1002/adma.201706311.

[27] Lv C, Krishnaraju D, Konjevod G, Yu H, Jiang H. Origami based mechanical metamaterials. Sci Rep 2014;4:5979. https://doi.org/10.1038/srep05979.

[28] Schenk M, Guest SD. Geometry of Miura-folded metamaterials. Proc Natl Acad Sci 2013;110:3276–81. https://doi.org/10.1073/pnas.1217998110.

[29] Miura K. New structural form of sandwich core. J Aircr 1975;12:437–41. https://doi.org/10.2514/3.44468.

[30] Zhou X, Wang H, You Z. Mechanical properties of Miura-based folded cores under quasi-static loads. Thin-Walled Struct 2014;82:296–310. https://doi.org/10.1016/j.tws.2014.05.001.

[31] Fischer S. Aluminium foldcores for sandwich structure application: Mechanical properties and FE-simulation. Thin-Walled Struct 2015;90:31–41. https://doi.org/10.1016/j.tws.2015.01.003.

[32] Lv Y, Zhang Y, Gong N, Li Z-X, Lu G, Xiang X. On the out-of-plane compression of a Miura-ori patterned sheet. Int J Mech Sci 2019;161-162:105022. https://doi.org/10.1016/j.ijmecsci.2019.105022.

[33] Zhang J, Lu G, Zhang Y, You Z. A study on ballistic performance of origami sandwich panels. Int J Impact Eng 2021;156:103925. https://doi.org/10.1016/j.ijimpeng.2021.103925.

[34] Li W, Zheng Q, Fan H, Ji B. Fabrication and mechanical testing of ultralight folded lattice-core sandwich cylinders. Engineering 2020;6:196–204. https://doi.org/10.1016/j.eng.2019.11.008.

[35] Du Y, Song C, Xiong J, Wu L. Fabrication and mechanical behaviors of carbon fiber reinforced composite foldcore based on curved-crease origami. Compos Sci Technol 2019;174:94–105. https://doi.org/10.1016/j.compscitech.2019.02.019.

[36] Zhang J, Karagiozova D, You Z, Chen Y, Lu G. Quasi-static large deformation compressive behaviour of origami-based metamaterials. Int J Mech Sci 2019;153–154:194–207. https://doi.org/10.1016/j.ijmecsci.2019.01.044.

[37] Karagiozova D, Zhang J, Lu G, You Z. Dynamic in-plane compression of Miura-ori patterned metamaterials. Int J Impact Eng 2019;129:80–100. https://doi.org/10.1016/j.ijimpeng.2019.02.012.

[38] Harris JA, McShane GJ. Metallic stacked origami cellular materials: additive manufacturing, properties, and modelling. Int J Solids Struct 2020;185–186:448–66. https://doi.org/10.1016/j.ijsolstr.2019.09.007.

[39] Meza LR, Zelhofer AJ, Clarke N, Mateos AJ, Kochmann DM, Greer JR. Resilient 3D hierarchical architected metamaterials. Proc Natl Acad Sci 2015;112:11502–7. https://doi.org/10.1073/pnas.1509120112.

[40] Kooistra GW, Deshpande V, Wadley HNG. Hierarchical corrugated core sandwich panel concepts. J Appl Mech 2007;74:259–68. https://doi.org/10.1115/1.2198243.

[41] Yin H, Huang X, Scarpa F, Wen G, Chen Y, Zhang C. In-plane crashworthiness of bio-inspired hierarchical honeycombs. Compos Struct 2018;192:516–27. https://doi.org/10.1016/j.compstruct.2018.03.050.

[42] Dong L. Mechanical response of Ti–6Al–4V hierarchical architected metamaterials. Acta Mater 2019;175:90–106. https://doi.org/10.1016/j.actamat.2019.06.004.

[43] Zhang L, Hu Z, Wang MY, Feih S. Hierarchical sheet triply periodic minimal surface lattices: design, geometric and mechanical performance. Mater Des 2021;209:109931. https://doi.org/10.1016/j.matdes.2021.109931.

[44] Ashby MF, Bréchet YJM. Designing hybrid materials. Acta Mater 2003;51:5801–21. https://doi.org/10.1016/S1359-6454(03)00441-5.

[45] Yan LL, Yu B, Han B, Chen CQ, Zhang QC, Lu TJ. Compressive strength and energy absorption of sandwich panels with aluminum foam-filled corrugated cores. Compos Sci Technol 2013;86:142–8. https://doi.org/10.1016/j.compscitech.2013.07.011.

[46] Han B, Qin K, Yu B, Wang B, Zhang Q, Lu TJ. Honeycomb-corrugation hybrid as a novel sandwich core for significantly enhanced compressive performance. Mater Des 2016;93:271–82. https://doi.org/10.1016/j.matdes.2015.12.158.

[47] Fan J, Zhang L, Wei S, Zhang Z, Choi S-K, Song Bo, et al. A review of additive manufacturing of metamaterials and developing trends. Mater Today 2021;50:303–28. https://doi.org/10.1016/j.mattod.2021.04.019.

[48] Gu D, Shi X, Poprawe R, Bourell DL, Setchi R, Zhu J. Material-structure-performance integrated laser-metal additive manufacturing. Science 2021;372. https://doi.org/10.1126/science.abg1487.

[49] Zhao Z, Han B, Wang X, Zhang Q, Lu TJ. Out-of-plane compression of Ti-6Al-4V sandwich panels with corrugated channel cores. Mater Des 2018;137:463–72. https://doi.org/10.1016/j.matdes.2017.10.055.

[50] Prabhakar P, Sames WJ, Dehoff R, Babu SS. Computational modeling of residual stress formation during the electron beam melting process for Inconel 718. Addit Manuf 2015;7:83–91. https://doi.org/10.1016/j.addma.2015.03.003.

[51] Raghavan S, Zhang B, Wang P, Sun C-N, Nai MLS, Li T, et al. Effect of different heat treatments on the microstructure and mechanical properties in selective laser melted INCONEL 718 alloy. Mater Manuf Process 2017;32:1588–95. https://doi.org/10.1080/10426914.2016.1257805.

[52] LeBrun T, Nakamoto T, Horikawa K, Kobayashi H. Effect of retained austenite on subsequent thermal processing and resultant mechanical properties of selective laser melted 17–4 PH stainless steel. Mater Des 2015;81:44–53. https://doi.org/10.1016/j.matdes.2015.05.026.

[53] Abramowicz W, Jones N. Dynamic progressive buckling of circular and square tubes. Int J Impact Eng 1986;4:243–70. https://doi.org/10.1016/0734-743X(86)90017-5.

[54] Côté F, Deshpande VS, Fleck NA, Evans AG. The out-of-plane compressive behavior of metallic honeycombs. Mater Sci Eng A 2004;380:272–80. https://doi.org/10.1016/j.msea.2004.03.051.

[55] Han B, Yan LL, Yu B, Zhang QC, Chen CQ, Lu TJ. Collapse mechanisms of metallic sandwich structures with aluminum foam-filled corrugated cores. J Mech Mater Struct 2014;9:397–425. https://doi.org/10.2140/jomms.2014.9.397.